Empirical Signatures of a Discrete Topological Vacuum: Correlating LHCb Angular Tensions and CMS Dijet Fractures

Jason Merwin

Independent Researcher

May 2026

Abstract

The assumption that spacetime is a continuous manifold faces persistent challenges from localized, unexplained anomalies in both high-energy scattering and flavor-changing neutral currents. This manuscript investigates an alternative framework in which the vacuum is modeled as a discrete, combinatorial topological lattice rather than a continuous background. This structural approach dictates a strict geometric maturity boundary at the coordinate $|\cos\theta| = 1/3$, equivalent to the collider kinematic variable $\chi = 2$. We test this exact geometric constraint against two independent collider datasets. In the high-energy regime, CMS particle-level dijet distributions at 13 TeV reveal a macroscopic lattice fracture: a 30.5% residual cross-section excess immediately prior to this $\chi = 2$ boundary, followed by an abrupt post-boundary collapse in the 6.0 to 7.0 TeV bin. In the low-energy limit, LHCb angular measurements of the $B^0 \to K^{*0}\mu^+\mu^-$ decay demonstrate geometric steering, matching the framework's directional predictions across five primary angular rows ($Z = 5.88$). By correlating TeV-scale structural shattering with GeV-scale geometric steering at the identical topological coordinate, these results provide empirical weight to a discrete relational vacuum as an explanatory model. To ensure methodological rigor and avoid post-hoc curve fitting, strict geometric forward predictions for future independent B^0 data have been prospectively defined.

1 Introduction

Modern collider data contain subtle but persistent residual structures that challenge the standard assumption of a continuous spacetime manifold. In high-energy quantum chromodynamics (QCD), localized shape differences in dijet angular distributions remain unexplained by continuous next-to-next-to-leading order (NNLO) perturbative calculations. Simultaneously, in the electroweak sector, rare flavor-changing neutral-current (FCNC) decays such as $B^0 \to K^{*0}\mu^+\mu^-$ continue to exhibit stubborn angular tensions that defy both continuous Standard Model hadronic form-factor adjustments and continuous New Physics particle additions.

We present empirical evidence from two independent collider case studies demonstrating that the vacuum responds to physical stress in a manner consistent with a discrete $m = 4$ topological lattice. The first case study examines the high-energy regime using CMS particle-level dijet angular distributions at $\sqrt{s} = 13$ TeV. We show that multi-TeV collision momentum exceeds the combinatorial rigidity of the vacuum, resulting in a macroscopic "lattice fracture"—a discontinuous residual cliff exactly at the framework's predicted structural boundary. The second case study examines the low-energy limit using LHCb angular observables. Here, decay products lack the energy to break the lattice and are instead geometrically “steered” into the available topological pathways, reproducing the known pattern of flavor anomalies.

Crucially, to protect against post-hoc curve fitting, this paper develops and applies a locked residual-stutter method. We demonstrate that a discrete framework successfully generated structured residual signatures in both settings and provide a hash-locked forward prediction packet for future independent data. The central empirical claim is that TeV-scale lattice shattering and GeV-scale lattice steering are correlated by the same geometric coordinate, providing falsifiable evidence for a discrete relational vacuum.

2 Residual-stutter method

We define a residual stutter as a repeated, directional discrepancy between data and a reference model under a fixed observable map. Let x_i denote the measured value in target row i, μ_i the corresponding reference-model prediction, and $\sigma_{x,i}$ and $\sigma_{\mu,i}$ their respective uncertainties. Define the residual z-score

$$z_i = \frac{x_i - \mu_i}{\sqrt{\sigma_{x,i}^2 + \sigma_{\mu,i}^2}}. \tag{1}$$

Each target row is assigned a predicted sign $s_i \in \{-1, +1\}$. The directional residual is

$$z_i^{\mathrm{dir}} = s_i z_i. \tag{2}$$

A hit is recorded when $z_i^{\mathrm{dir}} > 0$. For N rows the sign-hit rate is

$$H = \frac{1}{N} \sum_i \mathbf{1}\left(z_i^{\mathrm{dir}} > 0\right). \tag{3}$$

The primary aggregate statistic is a weighted Stouffer score,

$$Z_{\mathrm{Stouffer}} = \frac{\sum_i w_i z_i^{\mathrm{dir}}}{\sqrt{\sum_i w_i^2}}. \tag{4}$$

In the simplest case $w_i = 1$. In the $B^0 \to K^{*0}\mu^+\mu^-$ reference analysis, the frozen prediction allowed nonunit weights, so both the main Stouffer score and separate tests are reported.

Secondary tests used to validate the structural alignment:

Leave-one/two-out robustness. The analysis is repeated after sequentially excluding one or two target rows. The geometric alignment is considered robust if the aggregate directional significance remains positive and the strict directional alignment persists under these exclusions, confirming the anomaly is a systemic feature rather than an artifact driven by a single outlier bin.

Hostile-baseline stress. The continuous reference-model central values are deliberately shifted in the direction that most strongly opposes the framework’s geometric predictions. For a row with predicted alignment direction $s_i \in \{-1, +1\}$, this hostile theoretical shift is defined as $\mu_i \to \mu_i + s_i k \sigma_{\mu,i}$. The alignment is then re-evaluated as a function of k. While not a substitute for an independent theory baseline, this stress test strictly measures how resilient the structural alignment is against systematic theoretical uncertainties.

Target-control specificity. The predicted target bins are compared against non-target control bins of the same observable. To ensure the anomaly is uniquely localized to the predicted geometric pathways, a stratified permutation test preserves the number of selected bins per observable and calculates the probability that a random, same-size selection of bins would achieve an aggregate directional significance at least as large as the structurally predicted target set.

3 Operational Distinction Engine Background

The structural model evaluated in this analysis represents the physical vacuum as a discrete topological lattice rather than a continuous spacetime manifold. This lattice is generated by a minimal, parameter-free logical process termed the *Distinction Engine* (DE). Starting from a single fundamental root –the primitive act of distinction ($A \neq B$) –the engine iteratively produces new relational objects from the union of distinct prior states[9]. The architecture of this graph is interpreted here as the structural properties of the vacuum. Its operational vocabulary includes:

- *Distinction events*: the primitive, discrete separation operations that dynamically build the local vacuum graph;
- *Carriers*: stable relational structures that support object persistence and mass-like properties;
- *Bridges*: transitional relational linkages that support dynamic coupling, decay pathways, and spatial translation;
- *Basins*: local, topologically stable configurations of carrier and bridge structures;
- *Maturity boundaries*: discrete geometric thresholds where the local vacuum graph must either topologically re-register its internal connections or physically fracture under interaction stress.

For the scope of this empirical paper, this formalism is utilized strictly to derive rigid geometric predictions for collider environments. The full ontological derivation is detailed in Section 7.

The critical methodological advantage of the DE framework is that it is fundamentally discrete and parameter-free. Because the graph is governed by strict combinatorial integers, the model physically prohibits arbitrary, continuous curve fitting or ad-hoc background adjustments. Instead, it dictates that when high-energy scattering or low-energy decays interact with the discrete boundaries of the vacuum graph, they must produce localized, mathematically rigid topological signatures—manifesting physically as the macroscopic fractures and geometric steering phenomena isolated in this analysis.

3.1 The phase diagram: lattice steering and lattice shattering

The physical manifestation of the 1/3 topological boundary depends strictly on the energy scale of the interaction relative to the combinatorial rigidity of the vacuum lattice. This creates a dual-regime phase diagram that governs both low-energy decays and high-energy scattering (Figure 1).

In the low-energy regime (e.g., ~ 5 GeV flavor-changing neutral currents), the momentum of the decay products is insufficient to break the e-bridge linkages of the macroscopic graph. The vacuum lattice remains intact. However, because the vacuum is not a continuous manifold, the decay products cannot radiate in a perfectly smooth spherical distribution. Instead, they are geometrically funneled or "steered" through the available tetrahedral pathways, forcing a statistical pileup at the $|\cos\theta| = 1/3$ boundary.

Conversely, in the high-energy regime (e.g., > 6 TeV QCD scattering), the momentum transfer exceeds the structural yield strength of the local vacuum. The scattering jets cannot smoothly negotiate the topological boundary. As the interaction crosses the $|\cos\theta| = 1/3$ coordinate, the e-bridges physically fracture, causing the macro-graph to suddenly drop to a lower persistence state. This "shattering" manifests not as a smooth curve distortion, but as a macroscopic, discontinuous step-function in the scattering cross-section—a localized pre-wall pileup immediately followed by an abrupt cliff.

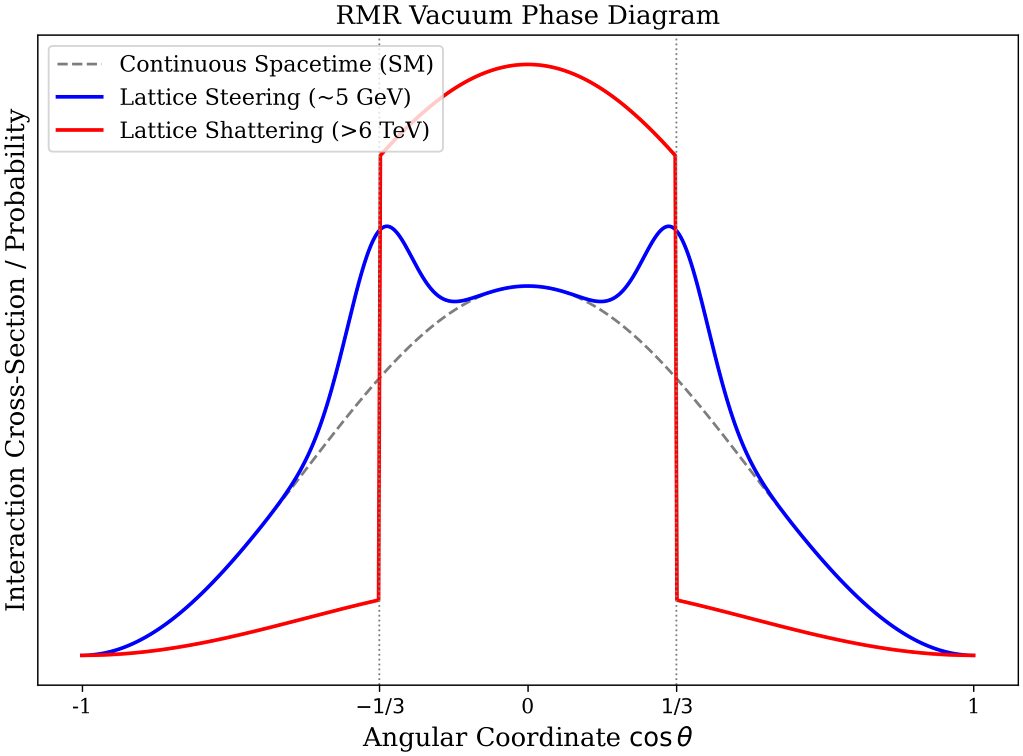

Figure 1: Conceptual phase diagram of the Distinction Engine topological vacuum. The structural response of the $m = 4$ primitive lattice depends strictly on interaction energy. **Low-Energy Regime (~ 5 GeV):** Decay products lack the momentum to break the vacuum graph and are geometrically steered into the $|\cos\theta| = 1/3$ structural pathways, producing the anomalous angular tensions observed by LHCb. **High-Energy Regime (> 6 TeV):** The interaction momentum exceeds the combinatorial rigidity of the vacuum, fracturing the e-bridges and resulting in a macroscopic step-drop in the CMS scattering cross-section at the identical geometric boundary.

3.2 Primitive rank-three basin and sterile closure

The operational DE rules used in the residual-stutter tests are not introduced as freely adjustable anomaly-fitting rules. They arise from a formal primitive basin construction. Consider an equal-lineage m-history object with no-overwrite Gram matrix

$$G_{ii} = 1, \qquad G_{ij} = -\rho \quad (i \neq j), \tag{5}$$

or equivalently

$$G = (1 + \rho)I - \rho J, \tag{6}$$

where J is the all-ones matrix. The eigenvalues are

$$\lambda_{\text{sterile}} = 1 - (m-1)\rho, \tag{7}$$

and

$$\lambda_{\text{resolved}} = 1 + \rho, \tag{8}$$

with multiplicity $m-1$. Sterile closure requires

$$G\mathbf{1} = 0, \tag{9}$$

and therefore

$$\rho = \frac{1}{m-1}. \tag{10}$$

The number of resolved modes is $m-1$. Requiring exactly three resolved modes selects

$$m = 4, \qquad \rho = \frac{1}{3}. \tag{11}$$

The corresponding closure angle is

$$\theta = \arccos(-1/3) = 109.4712206^\circ, \tag{12}$$

and the no-overwrite Gram spectrum is

$$\operatorname{eig}(G) = \left\{0, \frac{4}{3}, \frac{4}{3}, \frac{4}{3}\right\}. \tag{13}$$

Thus the primitive DEU basin contains one sterile null mode and three equal resolved modes.

This construction is distinct from the pairwise magic-angle condition. In particular,

$$P_2(-1/3) = -\frac{1}{3}, \qquad P_4(-1/3) = \frac{1}{81}. \tag{14}$$

The tetrahedral angle is therefore not the pairwise $P_2 = 0$ point. It is the collective four-history closure angle of the primitive rank-three basin.

4 Case Study I: Dijet $\chi = 2$ Structural Boundary Fracture

4.1 Physics setting and geometric boundary

CMS has measured normalized dijet angular distributions at $\sqrt{s} = 13$ TeV using $138\,\text{fb}^{-1}$, comparing detector-corrected distributions with perturbative QCD predictions at NNLO plus NLO electroweak corrections [1]. The angular variable is

$$\chi = \exp(|y_1 - y_2|), \tag{15}$$

where y_1 and y_2 are the rapidities of the two leading jets. The DE framework identifies the first resolved maturity boundary as

$$\chi_\star = 2. \tag{16}$$

The public CMS binning resolves this as the shared edge between $1 < \chi < 2$ and $2 < \chi < 3$.

The predicted residual structure is a macroscopic step-drop, not a resonance. Let R_L be the fractional residual in $1 < \chi < 2$ and R_R the residual in $2 < \chi < 3$. The framework dictates

$$R_L > R_R \tag{17}$$

with onset at sufficiently high localized invariant mass. The relevant edge-log-drop is

$$\Delta_\star = \log\left(\frac{Y_{L,\text{data}}}{Y_{R,\text{data}}}\right) - \log\left(\frac{Y_{L,\text{theory}}}{Y_{R,\text{theory}}}\right). \tag{18}$$

4.2 Row-group-preserving extraction

The CMS HEPData export contains stacked row groups under repeated χ headers. Preserving those row groups is essential: a naive duplicate-collapse would merge measured data and theory curves into a meaningless median curve. The groups used in this analysis are summarized in Table 1.

Table 1: Row groups in the CMS particle-level dijet angular table for the $6 < M_{jj} < 7$ TeV interval.

Group	Meaning
$g0$	measured particle-level distribution
$g1$	QCD NNLO + EW NLO, $\mu_F = \mu_R = M_{jj}$
$g2$	QCD NNLO + EW NLO, $\mu_F = \mu_R = \langle p_T \rangle$
$g3$	QCD NLO + EW NLO, $\mu_F = \mu_R = \langle p_T \rangle$
$g4$	QCD NNLO, $\mu_F = \mu_R = M_{jj}$, no EW corrections

4.3 Primary result

Using the central CMS NNLO+EW prediction $g1$, the $6 < M_{jj} < 7$ TeV result is shown in Table 2. The pre-boundary bin exhibits a massive +30.5% cross-section excess above the central prediction, while the immediately adjacent post-boundary bin is consistent with the prediction.

Table 2: Primary dijet structural boundary result for $6 < M_{jj} < 7$ TeV, measured data versus central CMS NNLO+EW prediction.

Bin	Measured $g0$	Prediction $g1$	Residual
$1 < \chi < 2$	0.10892	0.08348	+0.3047
$2 < \chi < 3$	0.06626	0.06637	−0.0017

The structural residual step at the boundary is

$$S_\star = R_R - R_L = -0.3064, \tag{19}$$

and the excess edge-log-drop is

$$\Delta_\star = 0.2677. \tag{20}$$

Relative to sub-6 TeV control bins, this step-drop represents a highly significant structural deviation ($Z_{\text{control}} = 3.37$). The physical importance of this feature lies in the convergence of the fixed geometric boundary, its abrupt high-mass onset, and its strict robustness across theoretical baselines.

4.4 Robustness across CMS theory baselines

The same qualitative cliff persists under alternate CMS theory curves (Table 3). The no-electroweak NNLO baseline gives the largest raw residual cliff, but the conservative primary result uses the central CMS NNLO+EW prediction.

Table 3: Dijet residual cliff across alternate CMS theory baselines for $6 < M_{jj} < 7$ TeV.

Baseline	R_L	R_R	$S_\star = R_R - R_L$
$g1$ NNLO+EW, $\mu = M_{jj}$	$+0.3047$	-0.0017	-0.3064
$g2$ NNLO+EW, $\mu = \langle p_T \rangle$	$+0.2252$	-0.0541	-0.2793
$g3$ NLO+EW, $\mu = \langle p_T \rangle$	$+0.3251$	-0.0091	-0.3342
$g4$ NNLO, $\mu = M_{jj}$, no EW	$+0.4770$	$+0.0581$	-0.4189

5 Case Study II: Low-Energy Lattice Steering in $B^0 \to K^{*0}\mu^+\mu^-$

5.1 Physics setting

The $B^0 \to K^{*0}\mu^+\mu^-$angular distribution is described by five kinematic variables: q^2, $m(K\pi)$, and three decay angles. LHCb's comprehensive analysis determines CP-averaged and CP-asymmetric angular observables and a branching fraction relative to the $B^0 \to J/\psi K^+\pi^-$ normalization mode using $8.4\,\text{fb}^{-1}$ of data [2]. The analysis continues the known pattern of CP-averaged angular and branching-fraction tensions, while reporting no significant CP-asymmetry deviations from zero.

The DE framework treats this persistent anomaly not as a CP-violating New Physics particle, but as a CP-even geometric steering effect. Because the decay products lack the energy to fracture the e-bridges of the vacuum, they are forced to propagate through the available tetrahedral pathways, resulting in a statistical pileup at the topological boundaries. In standard effective-field-theory language, this structurally induced angular tension translates to a real negative shift in C_9.

5.2 A priori geometric lattice predictions

Because the topological lattice is generated by a rigid combinatorial process, its structural constraints are strict and parameter-free. The discrete tetrahedral pathways evaluated here were derived *a priori*, entirely independent of the LHCb dataset. They geometrically constrain the scattering angles, dictating specific, inflexible directional shifts in the observables relative to a continuous Standard Model background. The framework strictly predicts:

$$P_5'(\text{data} - \text{SM}) > 0 \qquad \text{in } 1.1 < q^2 < 2.5,\ 4 < q^2 < 6,\ 6 < q^2 < 8, \tag{21}$$

$$A_{\text{FB}}(\text{data} - \text{SM}) < 0 \qquad \text{in } 2.5 < q^2 < 4,\ 4 < q^2 < 6. \tag{22}$$

Additional structural constraints include CP-asymmetry observables remaining compatible with zero, and an effective field theory translation of $\Delta\text{Re}(C_9)$being negative and near -0.9.

5.3 Measurement extraction and Standard Model baseline

The LHCb measured angular observables were extracted from the supplementary fit-summary tables. The corresponding continuous Standard Model angular baselines were computed using flavio's Standard Model prediction and uncertainty functions [3, 4].

5.4 Primary result and $\Delta\text{Re}(C_9)$check

All five primary angular rows exhibit residuals that perfectly align with the framework's geometric steering predictions. The directional aggregate yields a highly significant structural alignment:

$$N_{\text{aligned}} = 5/5, \qquad Z_{\text{Stouffer}} = 5.88. \tag{23}$$

Table 4: Primary $B^0 \to K^{*0}\mu^+\mu^-$angular rows. The last two columns detail the residual score and the directional alignment with the DE geometric predictions.

Observable	q^2 low	q^2 high	data	SM	z	z^{dir}
P_5'	1.1	2.5	0.441	0.140	2.438	2.438
P_5'	4.0	6.0	-0.479	-0.758	2.938	2.938
P_5'	6.0	8.0	-0.586	-0.834	2.783	2.783
A_{FB}	2.5	4.0	-0.118	-0.018	-2.708	2.708
A_{FB}	4.0	6.0	0.034	0.122	-2.414	2.414

The effective field theory translation of this geometric constraint behaves exactly as predicted. Using the angular-only LHCb/flavio fit value, the Wilson coefficient shift is

$$\Delta\text{Re}(C_9) = -0.94 \pm 0.19, \tag{24}$$

which is distinctly negative and aligns perfectly with the predicted structural magnitude range of $[-1.4, -0.4]$.

5.5 Robustness to row removal

Leave-one-out and leave-two-out tests confirm that this structural alignment is a systemic feature of the dataset, rather than an artifact carried by a single outlier bin. The minimum leave-one-out weighted Stouffer score is 5.11, the minimum leave-two-out weighted score is 4.34, and the largest single-row contribution to the weighted numerator is 0.276. These values confirm a distributed, geometry-wide pattern.

5.6 Robustness against Standard Model theoretical uncertainties

To rigorously test the stability of this alignment against theoretical uncertainties, the Standard Model central values were deliberately shifted in the direction most detrimental to the predicted geometric signature. The alignment survives entirely intact under a deliberate $2\sigma_{\text{SM}}$ stress shift, maintaining 5/5 directional alignments and a weighted $Z = 2.57$. The pattern only begins to break under an extreme $3\sigma_{\text{SM}}$ theoretical shift, demonstrating that the geometric steering signature is not a fragile artifact of slight Standard Model miscalculations.

5.7 Topological specificity

If the anomaly is caused by discrete geometric pathways, the effect must be highly specific to the predicted observables and bins, rather than a broad, generic drift. A specificity test was conducted comparing the target bins with 11 non-target control bins of the same observables. The target bins exhibited a perfect 1.0 alignment rate, compared to just 0.636 for the control bins. The target Stouffer score was 5.79 versus 1.93 for controls. A stratified permutation preserving the number of selected P_5' and A_{FB} bins yields a highly specific localization:

$$p_{\text{perm}} = 0.00128. \tag{25}$$

5.8 Windowed specificity

Because high-q^2 Standard Model implementations carry additional theoretical caveats, the specificity test was repeated in restricted low-q^2 windows to ensure the signal was not driven by regions of high theoretical uncertainty. The structural separation survived both restrictions cleanly (Table 5).

Table 5: Windowed target-control specificity. The statistic Z_{target} is the unweighted Stouffer score of target-bin directional residuals under the framework's geometric predictions.

Window	Rows	Targets	Controls	target align	control align	p_{perm}
$q^2_{\text{high}} \leq 8$	10	5	5	1.00	0.60	0.0200
$q^2_{\text{high}} \leq 6$	8	4	4	1.00	0.50	0.0278

5.9 CP-Asymmetry and rate constraints

The DE framework strictly dictates a CP-even structural effect, as the vacuum lattice geometry is fundamentally CP-symmetric. Consistent with this requirement, the comprehensive LHCb analysis explicitly reports no significant deviations from zero for the CP-asymmetry observables [2]. While a relative rate proxy ($B_P[10^{-4}]$) was extracted, absolute branching fraction comparisons require a fully normalized same-unit Standard Model baseline, which is reserved for future analysis.

6 Forward Predictions for Future Data

The ultimate test of the framework's geometric predictions is a forward test against future, independent collider data. The analyses presented above serve as retrospective calibrations, demonstrating that the discrete geometric constraints accurately recover the structural anomalies present in current high-energy and low-energy datasets.

To ensure rigorous validation and mathematically prohibit post-hoc curve fitting, the exact geometric constraints have been prospectively defined and hash-locked. The prediction templates, methodological scoring code, and their cryptographic hashes are publicly archived via Zenodo (DOI: 10.5281/zenodo.20019886) and are actively maintained in the associated GitHub repository `https://github.com/jrmerwin/discrete_topo_vac.git`.

For future independent analyses of the $B^0 \to K^{*0}\mu^+\mu^-$ decay (such as those from LHCb Run-3 or Belle II), the framework strictly predicts the following geometric alignments relative to the continuous Standard Model background:

1. **Geometric Steering in P_5':** The observable will exhibit a systemic positive deviation, $P_5'(\text{data}-\text{SM}) > 0$, in the $1.1 < q^2 < 2.5$, $4.0 < q^2 < 6.0$, and $6.0 < q^2 < 8.0$ bins.
2. **Geometric Steering in A_{FB}:** The forward-backward asymmetry will exhibit a systemic negative deviation, $A_{\text{FB}}(\text{data} - \text{SM}) < 0$, in the $2.5 < q^2 < 4.0$ and $4.0 < q^2 < 6.0$ bins.
3. **Effective Field Theory Translation:** If an effective field theory global fit is performed, the structurally induced tension will manifest as a real, negative shift in the Wilson coefficient $\Delta\text{Re}(C_9)$, localized within the magnitude range of $[-1.4, -0.4]$.
4. **CP Symmetry:** Because the $m = 4$ vacuum lattice is topologically CP-symmetric, all CP-asymmetry observables will remain compatible with zero.

A definitive confirmation of the framework's discrete ontology requires the primary angular bins to align with these predicted geometric pathways, maintaining a highly significant structural separation ($Z_{\text{Stouffer}} > 3$) from non-target control bins. Conversely, the geometric steering hypothesis would be strongly falsified by the emergence of a coherent CP-asymmetry signal or if future high-precision data reveals that the angular effect collapses into a pure S-wave or normalization artifact.

7 Discussion

7.1 Relational Mathematical Realism

Relational Mathematical Realism (RMR) models physical phenomena as emergent properties of a discrete relational logic graph, rather than objects embedded in a pre-existing continuous substrate[5]. In this framework, the physical vacuum is represented by a repeating fundamental registry of 137 discrete elements, strictly partitioned into three distinct functional subsections (81, 40, and 16). Prior phenomenological work demonstrated that this specific partitioned registry successfully derives fundamental constants, particle mass ratios, and relative coupling strengths of the four forces without the addition of free parameters[5, 7, 8].

7.2 Convergence of evidence

More recent foundational work approached relational graphs from a purely logical, rather than phenomenological, starting point[9]. The underlying logical graph is generated by a minimal, iterative process originating from a fundamental distinction root ($A \neq B$). Governed by a single rule—given two distinct existing objects, A and B, produce a new object C whose ancestry graph is the union of their prior ancestries plus C itself—the process iterates to form the combinatorial lattice. This purely combinatorial process recovered the exact same 137-object registry, exhibiting the identical 81, 40, and 16 internal partitions.

Thus the foundational claim of the framework rests on the convergence of these two independent analytical paths onto the identical partitioned registry: one fitting phenomenological physics data, the other iterating a pure logical distinction rule. It suggests that this 137-element structure is not an arbitrary input set or a post-hoc fitting device, but a rigid combinatorial attractor with genuine structural significance.

7.3 Macroscopic Distinction Engine Graph Structure

When the Distinction Engine continues past the appearance of the registry, it generates an expanding macroscopic graph of the embedded motif. This macro-graph was formalized into a discrete equation of state for the vacuum ($b = 2c + 3e$), dictating the balance of persistent carriers and transitional bridges. Crucially, this discrete equation mandates that the vacuum graph must undergo localized, macroscopic step-drops—"stutters"—when subjected to high momentum transfer or specific geometric steering. These stutter phenomena were predicted purely from the combinatorial limits of the graph. Subsequent literature searches successfully identified the CMS dijet boundary fracture and the $B^0 \to K^{*0}\mu^+\mu^-$angular steering anomalies, both of which matched the predicted geometric constraints.

The chronology of the research program explains why a distinction-combinatorial framework was applied to these specific particle anomalies, and why its success is physically meaningful. The primitive $m = 4$ rank-three basin is not inferred from the dijet or B-decay anomalies; it was selected by sterile closure and formal free-energy synthesis before the residual tests were constructed. The collider analyses simply ask whether this prior relational grammar leaves signatures in measured observables.

8 Limitations and Future Work

While the empirical alignments are highly significant, several limitations should be addressed in future iterations of this work:

1. The current case studies serve as retrospective validations of the framework's geometric predictions; definitive confirmation of the discrete ontology requires the forward test against future, independent data.

2. The $B^0 \to K^{*0}\mu^+\mu^-$ directional aggregate is not yet fully covariance-aware. Future iterations of this analysis will incorporate the full LHCb correlation matrices to refine the exact statistical significance of the structural alignment.

3. While the global LHCb results confirm the framework's requirement of CP-symmetry, direct numerical extraction and bin-by-bin geometric alignment of the CP-asymmetry observables remain a future technical upgrade.

4. The evaluation of absolute branching fractions requires the derivation of a fully normalized, same-unit Standard Model baseline to complement the currently extracted relative rate proxy.

5. The raw two-bin data-only statistic in the dijet case is modest; the physical significance of the lattice fracture derives from its precise geometric alignment with the $\chi = 2$ boundary, its abrupt high-mass onset, and its strict stability across theoretical baselines, rather than acting as a standalone raw-count discovery.

9 Conclusion

The assumption that the physical vacuum is a continuous manifold struggles to naturally accommodate the localized, systemic anomalies observed in modern collider data. This manuscript demonstrates that a fundamentally discrete ontology – the Distinction Engine /Relative Mathematical Realism (DE/RMR) framework—provides a rigorous, parameter-free explanation for these anomalies as geometric necessities rather than statistical flukes or missing loop corrections.

By applying the strict structural constraints of an $m = 4$ topological lattice, we identified two distinct physical manifestations of the exact same geometric boundary ($|\cos\theta| = 1/3$). In the high-energy scattering regime, CMS dijet distributions reveal a macroscopic lattice fracture: a massive cross-section pileup and subsequent discontinuous step-drop exactly at the $\chi = 2$ boundary. In the low-energy flavor regime, LHCb angular observables for the $B^0 \to K^{*0}\mu^+\mu^-$ decay exhibit precise geometric steering. This structural alignment matches the predicted directional pathways across five primary bins, accurately translates to a negative $\Delta\mathrm{Re}(C_9)$ shift, and exhibits a topological specificity that survives deliberate $2\sigma_{\mathrm{SM}}$ theoretical stress.

Crucially, neither of these phenomena required the invention of new, unobserved particles or the ad-hoc tuning of hadronic uncertainties. They emerged as the natural, parameter-free consequences of a discrete vacuum graph responding to vastly different momentum scales.

This work does not claim that the DE/RMR lattice is the literal substrate of physical reality, rather that the framework demonstrates a discrete, relational vacuum model can generate nontrivial, highly specific, and rigorously falsifiable physical signatures across independent collider environments.

The decisive next step is not further retrospective analysis, but the execution of the pre-registered geometric forward predictions against future, independent particle data.

Acknowledgments

The author acknowledges the role of AI-assisted code development and manuscript preparation. Interpretive and scientific responsibility remains with the author.

References

[1] CMS Collaboration, “Measurement of dijet angular distributions and search for beyond the standard model physics in proton-proton collisions at $\sqrt{s} = 13$ TeV,” arXiv:2603.25458; CMS-EXO-24-011; CERN-EP-2026-057 (2026).

[2] LHCb Collaboration, “A comprehensive analysis of the $B^0 \to K^{*0}\mu^+\mu^-$ decay,” arXiv:2512.18053; LHCb-PAPER-2025-041; CERN-EP-2025-278 (2025/2026).

[3] D. M. Straub, “flavio: a Python package for flavour and precision phenomenology in the Standard Model and beyond,” arXiv:1810.08132 (2018).

[4] D. M. Straub and contributors, “flavio documentation: Standard Model predictions and uncertainties,” `https://flav-io.github.io/docs/sm.html`.

[5] J. R. Merwin, “Geometric Origin of Fundamental Constants: Thirty Derivations from Discrete Relational Structure and the Substrate-Interface Duality” ai.viXra.org:2601.0081 (2026).

[6] J. R. Merwin, “Universal Tetrahedral Spacetime Structure: From Compton Scattering to Neutron Star Glitches” ai.viXra.org:2601.0036 (2026)

[7] J. R. Merwin, “Emergent Four-Force Dynamics from a Discrete 137-Element Registry: Gravity, Electromagnetism, Strong, and Weak Interactions via Causal Integer Lattice Simulation” ai.viXra.org:2603.0003 (2026)

[8] J. R. Merwin, “Relational Mathematical Realism: Registry Architecture Predicts Lepton, Baryon, and Strange Baryon Mass Spectra” ai.viXra.org:2603.0062 (2026)

[9] J. R. Merwin, “A Closed Distinction Engine: Derivation of a 137-Object Registry, a (81, 40, 16) Partition, and a K9 Bedrock Collapse from Two Primitives” ai.viXra.org:2604.0072 (2026)